Revealing defects in crystalline lithium-ion battery electrodes by solid state NMR: applications to LiVPO4F

Robert J. Messinger, Michel Ménétrier, Elodie Salager, Adrien Boulineau, Mathieu Duttine, Dany Carlier, Jean-Marcel Ateba Mba, Laurence Croguennec, Christian Masquelier, Dominique Massiot, et al.

Revealing Defects in Crystalline Lithium-Ion Battery Electrodes by Solid-State NMR: Applications to $LiVPO_4F$

Robert J. Messinger,[1,2] Michel Ménétrier,[3,2,4] Elodie Salager,[1,2] Adrien Boulineau,[5,2] Mathieu Duttine,[3,2] Dany Carlier,[3,2] Jean-Marcel Ateba Mba[3,5,4] Laurence Croguennec,[3,2,4] Christian Masquelier,[6,2,4] Dominique Massiot,[1] Michaël Deschamps[1,2,*]

[1]CEMHTI, CNRS UPR 3079, Univ Orléans, F-45071, Orléans, France, [2]RS2E, French Network for Electrochemical Energy Storage, FR CNRS 3459, F-80039 Amiens, France, [3]ICMCB, CNRS UPR 9048, Univ. Bordeaux, 33600 Pessac, France, [4]ALISTORE-ERI, FR CNRS 3104, F-80039 Amiens, France, [5]Univ. Grenoble Alpes, F-38000, Grenoble, France and CEA, LITEN, F-38054 Grenoble, France, [6]LRCS, CNRS UMR 7314, Univ. Picardie Jules Verne, F-80039, Amiens, France

Supporting Information

ABSTRACT: Identifying and characterizing defects in crystalline solids is a challenging problem, particularly for lithium-ion intercalation materials, which often exhibit multiple stable oxidation and spin states as well as local ordering of lithium and charges. Here, we reveal the existence of characteristic lithium defect environments in the crystalline lithium-ion battery electrode $LiVPO_4F$ and establish the relative sub-nanometer-scale proximities between them. Well-crystallized $LiVPO_4F$ samples were synthesized with the expected tavorite-like structure, as established by X-ray diffraction (XRD) and scanning transmission electron microscopy (STEM) measurements. Solid-state ^7Li nuclear magnetic resonance (NMR) spectra reveal unexpected paramagnetic ^7Li environments that can account for up to 20% of the total lithium content. Multi-dimensional and site-selective solid-state ^7Li NMR experiments using finite-pulse radio-frequency-driven recoupling (fp-RFDR) establish unambiguously that the unexpected lithium environments are associated with defects within the $LiVPO_4F$ crystal structure, revealing the existence of dipole-dipole-coupled defect pairs. The lithium defects exhibit local electronic environments that are distinct from lithium ions in the crystallographic $LiVPO_4F$ site, which result from altered oxidation and/or spin states of nearby paramagnetic vanadium atoms. The results provide a general strategy for identifying and characterizing lithium defect environments in crystalline solids, including paramagnetic materials with short ^7Li NMR relaxation times on the order of milliseconds.

INTRODUCTION

Lithium-ion batteries often use crystalline electrode materials that reversibly intercalate lithium ions within their structures upon electrochemical cycling.[1] Local defects in crystalline lithium-ion intercalation materials can affect their bulk electrochemical properties, sometimes significantly, yet unambiguously identifying their existence and understanding their physicochemical origins are challenging. Solid-state $^{6,7}Li$ nuclear magnetic resonance (NMR) spectroscopy is sensitive to the local electronic and magnetic environments of lithium atoms and hence is well suited to characterize structural defects and local disorder in lithium-ion battery materials.[2,3] In particular, the presence of paramagnetic transition metal ions in most electrochemically active materials drastically affects the $^{6,7}Li$ NMR shifts, lineshapes, and relaxation times due to Fermi contact and electron-nucleus dipolar interactions between the lithium and unpaired electron spins. These interactions provide insights into the local chemistry and structures of lithium-ion battery materials,[2,4,5] including defects. For example, Dogan *et al.*[6] used correlated ^6Li NMR and electrochemical measurements to show that even dilute concentrations of lithium defects can have significant influences on the bulk electrochemical performance of the lithium- and manganese-rich transition metal oxide $0.5Li_2MnO_3{\bullet}LiMn_{0.5}Ni_{0.5}O_2$. Similarly, the local lithium environments associated with structural defects in battery electrode materials have been characterized by $^{6,7}Li$ NMR in non-stoichiometric transition metal oxides, such as lithium-deficient $Li_{1-z}Ni_{1+z}O_2$[7] and lithium-excess $Li_{1+x}Co_{1-x}O_2$[8,9].

The through-space proximities of lithium atoms in different environments, including defects, can be established by solid-state NMR experiments that measure or correlate magnetic dipole-dipole couplings between ^{6,7}Li nuclei. Currently, there are very few reports in the literature of solid-state NMR experiments that recouple dipolar interactions between ^{6,7}Li nuclei under magic-angle-spinning (MAS), which averages such interactions but is itself necessary to obtain high-resolution NMR spectra. Pourpoint *et al.*[10] applied the symmetry-based double-quantum dipolar recoupling technique POST-C7[11] to ^{6}Li nuclei on $Li_{1+x}V_{1-x}O_2$. Similarly, Murakami *et al.*[9] studied the local lithium environments in Li-excess $LiCoO_2$ by zero-quantum ^{7}Li finite-pulse radio frequency driven recoupling (fp-RFDR[12,13]), as well as double-quantum homonuclear rotary resonance (HORROR[14]). In addition to NMR correlation experiments, dipolar-mediated experiments such as ^{6}Li{^{7}Li} REDOR[15,16] and ^{6}Li{^{7}Li} cross-polarization (CP)-MAS-based measurements[16] have been applied to lithium-ion transport in garnet-type solid electrolytes.

Here, using multi-dimensional and site-selective solid-state ^{7}Li dipolar correlation NMR experiments, we reveal the existence of characteristic lithium defect environments in the crystalline lithium-ion battery electrode $LiVPO_4F$ and establish the relative sub-nanometer-scale proximities between them. $LiVPO_4F$[17-20] is capable of operating both as a high-voltage positive electrode (4.25 V vs. Li, V^{III}/V^{IV}) and as a negative electrode (1.8 V vs. Li, V^{II}/V^{III}); when used as a positive electrode material, it exhibits a theoretical capacity of 156 mAh/g and one of the highest energy densities currently known among polyanionic compounds (655 Wh/kg).[21] For $LiVPO_4F$ samples that are well crystallized in the expected tavorite-like structure, as established by XRD and scanning transmission electron microscopy (STEM) measurements, solid-state ^{7}Li NMR measurements reveal unexpected lithium environments that can account for up to 20% of the total lithium content. 2D ^{7}Li{^{7}Li} fp-RFDR dipolar correlation NMR experiments prove unambiguously that such lithium environments are associated with defects in the $LiVPO_4F$ crystal structure, and crucially are not associated with amorphous impurity phases. Site-selective ^{7}Li fp-RFDR experiments were implemented for the first time, which establish proximities among the lithium defect environments at the scale of dipole-dipole-coupled defect pairs. The results highlight that ^{7}Li fp-RFDR dipolar correlation NMR experiments can be used to establish the proximities of lithium atoms in different environments, including defects, even for paramagnetic lithium-ion battery electrodes with fast ^{7}Li NMR relaxation times on the order of milliseconds.

EXPERIMENTAL SECTION

Materials. $LiVPO_4F$ samples were prepared using a two-step solid-state synthesis as described in Ateba Mba *et al.*[19] Carbon-coated VPO_4 (5 wt. % carbon) was first synthesized as an intermediate precursor by a carbothermal route. Stoichiometric quantities of V_2O_5 and $NH_4H_2PO_4$ were ball-milled with carbon (C_{sp}), pressed into a solid pellet, pre-treated at 300 °C for 8 h under argon flow, ground, and then heated to 800 °C for 10 h under argon flow. The resulting carbon-coated VPO_4 was subsequently pressed into a solid pellet with stoichiometric quantities of LiF and heated to 750 °C for 1 h within a sealed gold tube in an argon-filled glovebox. For $LiVPO_4F$ "sample A," the actual carbon content of the intermediate carbon-coated VPO_4 was measured by thermogravimetric analyses, revealing a slight excess of carbon. A precise stoichiometric mixture between VPO_4 and LiF was prepared accordingly. For $LiVPO_4F$ "sample B," the carbon-coated VPO_4 intermediate was assumed to contain the expected amount of VPO_4 (95 wt. %).

X-ray diffraction. XRD patterns were acquired using a Siemens D5000 diffractometer equipped with a detector using energy discrimination and Cu Kα radiation. Measurements were conducted in the 5 – 120° ($2\theta_{Cu}$) angular range with increments of 0.02° ($2\theta_{Cu}$) at a constant counting time of 15 s. Analyses of the XRD data by the Le Bail and Rietveld methods were performed as described in Ateba Mba *et al.*[19]

Transmission electron microscopy. Scanning transmission electron microscopy (STEM) images were recorded using a FEI Titan Ultimate microscope equipped with a monochromator and double spherical aberration correctors (Cs) for both the probe-forming and the image-forming lenses. The microscope was operating at an accelerating voltage of 200 kV using a 20 mrad convergence semi-angle. STEM images were collected using a high-angle annular dark field detector, where inner and outer semi-angles were 60 and 180 mrad, respectively. Samples were suspended in dimethyl carbonate in an argon-filled glovebox, deposited onto a carbon-coated grid, and then transferred to the microscope with a vacuum transfer holder.

Nuclear magnetic resonance spectroscopy. Solid-state ^{7}Li NMR spectra were acquired on a Bruker AVANCE III 750 NMR spectrometer with a 17.62 T wide-bore superconducting magnet operating at 291.5 MHz for ^{7}Li nuclei. Bruker ^{1}H/X double-resonance MAS probeheads were used with 1.3-mm diameter zirconia rotors, where samples were rotated at 64 kHz MAS with N_2 gas. Sample temperatures were calibrated using $Pb(NO_3)_2$ as a chemical shift thermometer.[22] Variable-temperature NMR experiments were conducted by pumping N_2 gas through the probehead under temperature regulation. A ^{7}Li radiofrequency field strength of 250 kHz ($\pi/2$ pulse of 1.25 μs) was used for all broadband pulses. Recycle

delays of 50 ms were used for all ^{7}Li NMR experiments, during which all ^{7}Li nuclear spins undergoing paramagnetic interactions fully relaxed to thermal equilibrium. ^{7}Li NMR shifts were referenced to a 1 mol L^{-1} aqueous solution of LiCl.

Solid-state ^{7}Li Hahn spin-echo MAS spectra were acquired with a delay of one rotor period (15.625 μs) between the π/2 and π pulses. These experiments yield quantitative ^{7}Li signal intensities among the paramagnetic lithium environments because the total echo delay of two rotor periods (31.25 μs) between the π/2 pulse and signal acquisition was much smaller than the transverse T_2 relaxation times of the ^{7}Li environments. Quantitative decompositions of the NMR spectra were performed using the DMfit program.[23] ^{7}Li T_1 and T_2 NMR relaxation measurements were acquired using the saturation recovery and Hahn spin-echo pulse sequences, respectively.

2D ^{7}Li{^{7}Li} exchange spectroscopy (EXSY) (Figure 1a) and ^{7}Li{^{7}Li} fp-RFDR dipolar correlation (Figure 1b) NMR measurements were acquired with mixing times of 10 ms. The fp-RFDR π pulses were phase cycled according to the $(XY\text{-}8)_4^1$ super cycle,[24] where the ratio of the π pulse duration (2.5 us) to the rotor period (15.625 μs) was 0.16. All 2D NMR experiments were conducted using a rotor-synchronized parametric time increment t_1 of 15.625 μs for a total acquisition time of 3.125 ms in the indirect dimension. Hypercomplex (States) quadrature detection was used in the indirect dimension.[25] For all 2D NMR experiments, a spin-echo was added before signal acquisition to eliminate distortions due to probe ring-down.

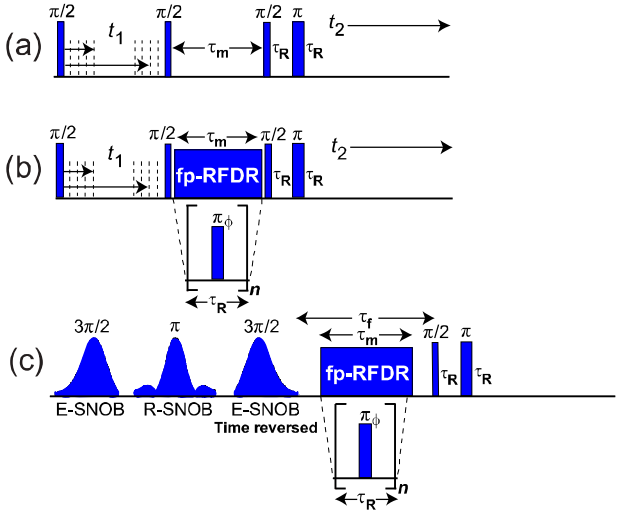

Figure 1. Solid-state (a) 2D ^{7}Li{^{7}Li} EXSY, (b) 2D ^{7}Li{^{7}Li} fp-RFDR dipolar correlation, and (c) 1D site-selective ^{7}Li fp-RFDR NMR pulse sequences. τ_1 and τ_2 are acquisition times in the indirect and direct dimension, respectively. τ_R, τ_m, and τ_f indicate one rotor period, the mixing time, and a fixed time to control for longitudinal relaxation, respectively.

Site-selective ^{7}Li fp-RFDR NMR experiments were implemented to probe the relative proximities among the different ^{7}Li environments (Figure 1c). SNOB-type pulses[26] were used to selectively excite the paramagnetic ^{7}Li signals due to their low bandwidth to pulse width products, which are desirable when manipulating short-lived NMR coherences. The initial 3π/2 excitation pulse and subsequent π refocusing pulse resulted in a cleaner selective excitation compared to either a 3π/2 or π/2 pulse alone. The site-selective ^{7}Li fp-RFDR NMR experiments were performed with mixing times ranging from 0 to 15 ms, where magnetization was stored along the longitudinal axis during a fixed time of 15 ms. The e-SNOB and r-SNOB selective pulse durations and strengths were optimized separately for each ^{7}Li signal. For example, for lithium environment '*a*' (full-width-half-max of 2.0 kHz), the 3π/2 e-SNOB and π r-SNOB pulses were 218.75 μs and 234.375 μs, respectively, with corresponding ^{7}Li field strengths of 3 kHz and 6.5 kHz.

RESULTS & DISCUSSION

The crystal structure of $LiVPO_4F$ is reported in Ateba Mba *et al.*,[19] which was obtained from analyzing neutron and laboratory X-ray diffraction data. $LiVPO_4F$ crystallizes into a tavorite-like structure that consists of chains of distorted VO_4F_2 octahedra sharing common fluorine atoms, where adjacent chains are connected by corner-sharing PO_4 tetrahedra. Lithium ions reside within the interstitial spaces and charge-compensate the paramagnetic vanadium atoms. Notably, $LiVPO_4F$ has only one crystallographic lithium site.[19,27,28] In our initial NMR experiments,[29] we reported an intense ^{7}Li NMR signal associated with $\mathbf{Li}VPO_4F$, consistent with a single crystallographic lithium site (in this notation, the letter in bold font represents atoms in the crystallographic site). Shortly after, Ellis *et al.*[20,29,30] reported that $LiVPO_4F$ had two crystallographic lithium sites; however, these results were based on synchrotron X-ray diffraction data only, a technique with low sensitivity to lithium due to its small atomic number. Recently, Kosova *et al.*[31] reported a single ^{6}Li MAS NMR signal that they associated with one crystallographic lithium site, in agreement with the structure reported in Ateba Mba *et al.*[19]

Powder XRD patterns acquired on the $LiVPO_4F$ samples (Figure 2) show intense, well-resolved reflections that indicate the materials are well crystallized. For $LiVPO_4F$ sample A (Figure 2a), Rietveld refinement of the structure from the XRD data (Figure S1 and table S1, Supporting Information) establishes that the material exhibits the expected tavorite-like crystal structure[19] and does not contain detectable crystalline impurities. The XRD pattern of sample B (Figure 2b) is very similar to the one of phase-pure sample A (Figure 2a), except that it shows additional weak reflections

associated with small concentrations of one or more unidentified impurities. Note that sample A was synthesized with the most accurate stoichiometry because the carbon content of the carbon-coated VPO_4 intermediate was separately quantified by thermogravimetric analysis. Thus, both of the $LiVPO_4F$ samples are well crystallized and exhibit well-defined tavorite-like structures, where sample A is phase-pure and sample B has minor impurities.

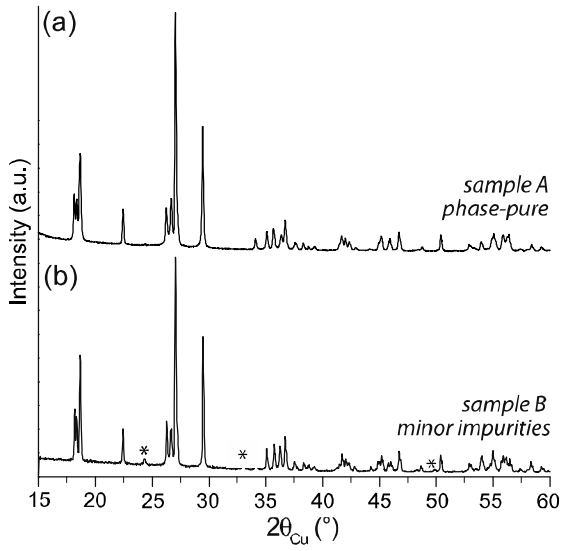

Figure 2. XRD patterns of (a) phase-pure $LiVPO_4F$ (sample A) and (b) $LiVPO_4F$ containing minor impurities (sample B). Reflections not associated with the crystal structure of $LiVPO_4F$ are indicated with asterisks.

STEM measurements were performed to examine the quality of periodic atomic ordering and visualize the crystal structure. A STEM image acquired on phase-pure $LiVPO_4F$ (sample A, Figure 3a) along the [010] zone axis shows periodic atomic ordering spanning several nanometers, consistent with the XRD analyses above. Typical $LiVPO_4F$ particle dimensions were on the order of 100's of nm (Figure 3a inset). An enlarged image of the same region (Figure 3b) reveals that the periodic atomic ordering agrees well with the crystal structure reported in Ateba Mba *et al.*[19] Similar STEM images corresponding to the [001] (Figure 3c) and [1-21] (Figure 3d) zone axes further confirm the high extents of atomic ordering in the material. Zoomed-out images of these same crystal orientations (Figure S2 and S3, Supporting Information) confirm that such atomic ordering persists over large length scales (>10 nm). Thus, STEM measurements reveal that $LiVPO_4F$ is well crystallized in the expected tavorite-like structure, corroborating the XRD measurements.

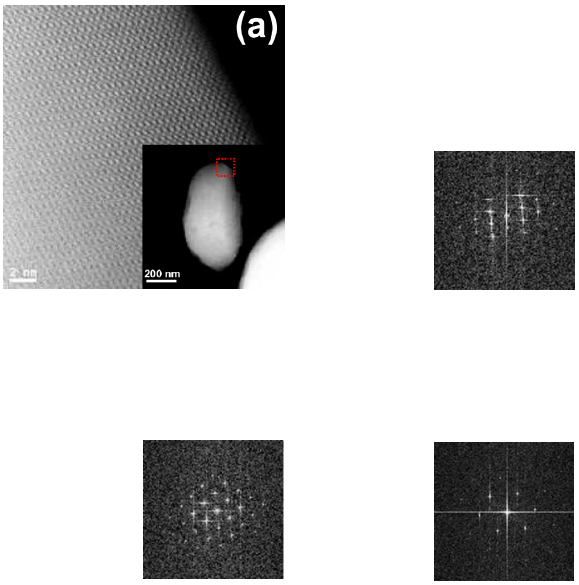

Figure 3. STEM images of phase-pure $LiVPO_4F$ (sample A) along different crystal orientations. (a) [010] zone axis, revealing periodic atomic ordering spanning several nanometers. *Inset:* $LiVPO_4F$ particle, showing the region (red box) from which the image was acquired. Zoomed-in images of the (b) [010], (c) [001], and (d) [1-21] zone axes, where an $LiVPO_4F$ unit cell is superimposed over each image. Vanadium, lithium, and phosphorous atoms are represented by blue, orange, and yellow spheres, respectively. *Insets:* corresponding fast Fourier transform patterns.

Electron energy loss spectroscopy (EELS) was conducted on phase-pure $LiVPO_4F$ (sample A) to examine the oxidation state of the vanadium atoms (Figure S4, Supporting Information). The vanadium L_2 and L_3 edges were examined, which correspond to electronic transitions from the $2p^{1/2}$ and $2p^{3/2}$ ground states, respectively, to energetically excited 3d states. The energy and intensity ratio of these two signals are directly related to the oxidation state of the vanadium atoms. The vanadium L_3 and L_2 edges are located at 517 eV and 521 eV, respectively. In accordance with previous studies,[27,28] such results establish the *average* V^{+3} valence state of the vanadium atoms, as expected in $LiVPO_4F$. Such results do not preclude the existence of vanadium in other oxidation states (e.g., V^{2+} or V^{4+}). Note that no iron impurities were detected by EELS, as the characteristic iron $L_{2,3}$ edge at 708 eV was not observed.[32].

While $LiVPO_4F$ exhibits long-range periodic atomic ordering corresponding to a well-defined average crystal structure, solid-state ^7Li NMR measurements reveal significant local disorder. A solid-state ^7Li spin-echo NMR spectrum of phase-pure $LiVPO_4F$ (sample A, Figure 4a) reveals an intense ^7Li signal at 113 ppm arising from lithium environments associated with the crystallographic Li site, $\mathbf{Li}VPO_4F$. Closer inspection of the isotropic ^7Li shifts (Figure 4b) reveals ^7Li NMR signals of unknown origin. Additional ^7Li signals are present at 4 ppm (labeled '*a*'), 82 ppm ('*b*'), and

180 ppm ('*c*'), as well as a broad, unresolved signal centered at ca. 155 ppm and a very weak signal at 45 ppm. The relative populations of lithium in these different environments can be quantified by comparing their relative ^{7}Li signal areas, summed over the entire spinning-sideband manifold. Here, the ^{7}Li signals associated with '*a*', '*b*', and '*c*' account for 4%, 3%, and 8% of the total lithium content, respectively. The broad, unresolved signal at ca. 155 ppm and weak signal at 44 ppm account for an additional 3% and 0.1% of the total lithium, respectively. Thus, ca. 18% of the lithium exhibits characteristic local environments that are different from crystallographic **Li**VPO4F. Note that additional ^{7}Li signals with weak signal intensities have been observed in other ^{7}Li NMR spectra of $LiVPO_4F$,[20,29,30] which appear to have similarities to those reported here, although they were not analyzed.

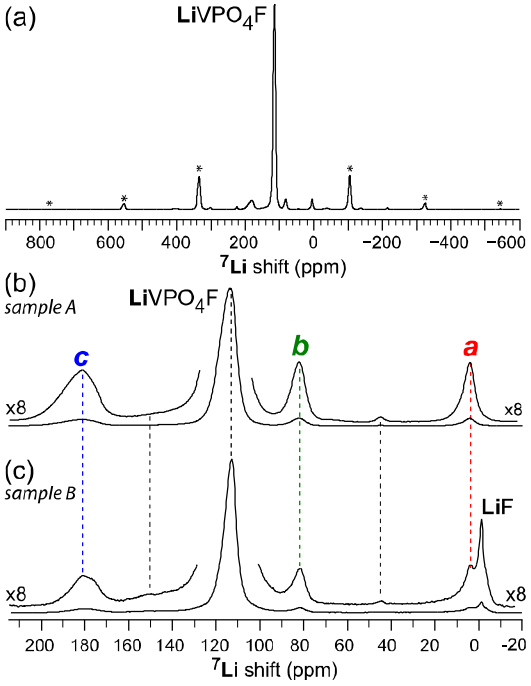

Figure 4. (a) Solid-state ^{7}Li spin-echo NMR spectrum of phase-pure $LiVPO_4F$ (sample A) acquired under conditions of 64 kHz MAS and 17.62 T at sample temperatures of 333 K. Asterisks indicate spinning sidebands. (b) Isotropic ^{7}Li shifts of the same NMR spectrum, revealing the existence of different characteristic ^{7}Li environments (e.g., '*a*', '*b*', and '*c*') in addition to crystallographic **Li**VPO_4F. (c) Isotropic ^{7}Li NMR shifts of $LiVPO_4F$ containing minor impurities (sample B), including **Li**F.

The solid-state ^{7}Li NMR shifts and relaxation times of the characteristic lithium environments '*a*', '*b*' and '*c*' establish that they are paramagnetic, a result of interactions with unpaired electron spins associated with nearby vanadium atoms. The ^{7}Li NMR shifts of the different lithium environments are outside the normal diamagnetic ^{7}Li shift range (ca. 5 to -5 ppm)[33], except for environment '*a*'.[34] While environment '*a*' is indeed paramagnetic (see below), its smaller ^{7}Li NMR shift is likely a result of competing Fermi contact shift mechanisms, which contribute opposite signs to its NMR shift.[2,4] In addition, the broad spinning-sideband manifold (Figure 4a) spans ca. 1500 ppm, a manifestation of strong interactions (predominantly dipolar) between the ^{7}Li and unpaired electron spins. The paramagnetic natures of the lithium environments are also consistent with their fast ^{7}Li NMR relaxation times (on the order of ms), which are dominated by stochastic fluctuating interactions (e.g., dipolar) between the ^{7}Li and unpaired electron spins. Crystallographic **Li**VPO_4F and environments '*a*', '*b*', and '*c*' exhibit very similar longitudinal ^{7}Li T_1 times of 7.1, 7.5, 6.8, and 7.7 ms, respectively, and transverse ^{7}Li T_2 times of 1.9, 2.1, 2.1, and 2.0 ms. Thus, like **Li**VPO_4F, the additional ^{7}Li environments '*a*', '*b*', and '*c*' are paramagnetic.

The presence of these characteristic ^{7}Li environments is reproducible among different samples, though their populations vary. A solid-state ^{7}Li spin-echo NMR spectrum acquired on $LiVPO_4F$ with minor impurities (sample B, Figure 4c) reveals the same additional ^{7}Li environments, '*a*', '*b*', and '*c*', as well as the broad, unresolved signal centered at ca. 155 ppm and very weak signal at 44 ppm. ^{7}Li signals associated with '*a*', '*b*', and '*c*' account quantitatively for 2%, 2%, and 4% of the total paramagnetic lithium content, respectively, and the broad signal at 150 ppm and weak signal at 44 ppm accounts for 2% and 0.2%. Thus, ca. 10% of the paramagnetic lithium is associated with local environments that are different from crystallographic **Li**VPO_4F. A resolved ^{7}Li signal is present at -1 ppm, assigned to residual **Li**F from the initial synthesis mixture. Both the magnitude of its ^{7}Li shift and its longer ^{7}Li T_1 NMR relaxation time (> 1 s) are consistent with its diamagnetic nature. The presence of this LiF impurity is further confirmed by solid-state ^{19}F measurements (see below). This LiF impurity was not detected by XRD, likely due to small crystallite sizes.

To further examine the different lithium environments in $LiVPO_4F$, solid-state ^{6}Li MAS NMR measurements were conducted at the same magnetic field strength and ultra-fast MAS rates as the solid-state ^{7}Li NMR experiments. A solid-state ^{6}Li spin-echo spectrum of $LiVPO_4F$ (sample B, Figure S5, Supporting Information) confirms the presence of the additional paramagnetic lithium environments. The ^{6}Li signals associated with environments '*a*', '*b*', and '*c*' have identical isotropic NMR shifts (in ppm), as expected, but interestingly appear with essentially identical spectral resolution, establishing that the ^{6,7}Li linewidths are a result of inherent distributions of local environments within the material. Under the conditions used here, ^{7}Li NMR experiments offer identical resolution with superior sensitivity, where anisotropic interactions (e.g., dipolar) that would otherwise reduce spectral resolution

are sufficiently averaged by ultra-fast MAS. Note that Kosova *et al.*[31] reported rather similar ^{6}Li NMR signals in their $LiVPO_4F/Li_3V_2(PO_4)_3$ composite material, with different relative signal intensities, which correspond well to the environments '*a*', '*b*', and '*c*' and the very weak signal at ca. 44 ppm. They assigned the latter signal, as well as ^{6}Li signals similar to environments '*b*' and '*c*', to the $Li_3V_2(PO_4)_3$ component; however, such assignments are not in agreement with the ^{6}Li signals reported for $Li_3V_2(PO_4)_3$ by Cahill *et al.*[35] We note that the extra signals are, rather, reminiscent of those reported for the parent compound $Li_3Fe_2(PO_4)_3$[36,37] As noted earlier, we did not detect the presence of iron impurities in our $LiVPO_4F$ samples using EELS.

Solid-state ^{19}F and ^{31}P MAS NMR measurements were conducted to investigate the local environments of the VPO_4F frameworks, which were acquired at low magnetic field strength (2.35 T) and fast MAS (28-30 kHz) to separate spinning sidebands. Crystallographically, $LiVPO_4F$ exhibits one fluorine site and one phosphorous site.[19] A solid-state ^{19}F spin-echo MAS NMR spectrum of phase-pure $LiVPO_4F$ (sample A, Figure S6a, Supporting Information) reveals a single ^{19}F signal at -1540 ppm with a broad spinning-sideband manifold, associated with the crystallographic F site, $LiVPO_4$**F**. Strong paramagnetic interactions likely obscure any resolution between ^{19}F environments; note that the fluorine atoms are covalently bonded to the paramagnetic vanadium atoms. A ^{19}F NMR spectrum of $LiVPO_4F$ with minor impurities (sample B, Figure S6b, Supporting Information) exhibits no significant differences, except for an additional ^{19}F signal at -204 ppm associated with the Li**F** impurity. A solid-state ^{31}P spin-echo MAS NMR spectrum of phase-pure $LiVPO_4F$ (sample A, Figure S7a, Supporting Information) exhibits an intense ^{31}P signal at 4000 ppm associated with the crystallographic P site, LiV**P**O_4F, where additional, unresolved ^{31}P signals overlap with the main signal, as well as its spinning sidebands. A ^{31}P NMR spectrum of $LiVPO_4F$ with minor impurities (sample B, Figure S7b, Supporting Information) exhibits a smaller population of these additional, un-resolved ^{31}P signals, consistent with the lower quantity of additional ^{7}Li environments (10% vs. 18%) between the materials. However, the resolution among ^{31}P signals associated with crystallographic LiV**P**O_4F and these additional phosphorous environments is too low to permit detailed analyses.

Given that the $LiVPO_4F$ samples are well crystallized, as measured by XRD and supported by STEM, it is natural to question whether the additional lithium environments measured by NMR are associated with defects within the $LiVPO_4F$ crystal structure, or with amorphous paramagnetic impurity phases. Below, using multi-dimensional and site-selective solid-state ^{7}Li NMR experiments based on ^{7}Li fp-RFDR, we show unambiguously that such additional lithium environments are associated with defects in the crystal structure.

2D ^{7}Li{^{7}Li} EXSY NMR measurements were performed to probe the possible chemical exchange of lithium between the different paramagnetic environments, which would provide evidence for their proximities. The exchange of lithium atoms between two different environments (e.g., crystallographic $\mathbf{Li}VPO_4F$ and '*a*') during the mixing time τ_m (Figure 1a) would result in correlated signals off the diagonal of the 2D spectrum. A 2D ^{7}Li{^{7}Li} EXSY spectrum acquired on $LiVPO_4F$ (sample B, Figure 5a) using a mixing time of 10 ms reveals no off-diagonal 2D signals between $\mathbf{Li}VPO_4F$ at 113 ppm and the other ^{7}Li environments, indicating no chemical exchange between them. The short ^{7}Li T_1 relaxation times of the paramagnetic lithium environments (all < 8 ms) prevented longer mixing times. Note that the star-shaped 2D signal associated with $\mathbf{Li}VPO_4F$ does not indicate chemical exchange among lithium ions in the crystallographic Li sites; a circular 2D signal would indicate exchange between them. This star-shaped pattern may be a result of the natural T_2 linewidth and significantly higher signal-to-noise ratio of the ^{7}Li signal of $\mathbf{Li}VPO_4F$ (>80%), compared to the other ^{7}Li signals (each <5%). Note also that ^{7}Li spin diffusion during the EXSY mixing time is suppressed by ultra-fast MAS (64 kHz), which would otherwise result in 2D signal correlations due to dipolar magnetization exchange. Thus, lithium ions in the additional environments do not exchange with crystallographic $\mathbf{Li}VPO_4F$, at least over 10 ms, leaving the question unanswered of whether such environments are associated with defects in the crystal structure or amorphous paramagnetic impurity phases.

The proximities of lithium in different environments can be probed directly by measuring their mutual ^{7}Li dipole-dipole couplings, a through-space magnetic interaction between nuclear spins. Homonuclear ^{7}Li-^{7}Li dipolar interactions, however, are effectively averaged by ultra-fast MAS, and consequently must be reintroduced by a suitable dipolar-recoupling pulse scheme. The fp-RFDR scheme[12,13], (based on the RFDR scheme[38]) uses rotor-synchronized and phase-cycled π pulses to reintroduce homonuclear dipolar couplings while magnetization is stored along the longitudinal axis (Figure 1b). Typical distances probed by fp-RFDR for non-quadrupolar nuclei (spin-1/2) are < 1 nm, and we expect similar sub-nanometer length scales to be probed between the weakly quadrupolar ^{7}Li nuclei (spin-3/2). For example, Shen *et al.*[24] demonstrate both theoretically and experimentally that fp-RFDR with a $(XY\text{-}8)4^1$ phase super-cycle can facilitate either direct or relayed dipolar transfer of magnetization among ^{13}C nuclei separated by distances of <5 Å. Note that in $LiVPO_4F$ crystal structure, the next-nearest lithium neighbor from a given lithium ion is 3.8 Å away, while

within a 5 Å coordination sphere, 4 other lithium ions are expected.

A 2D ^{7}Li{^{7}Li} fp-RFDR dipolar correlation NMR spectrum acquired on LiVPO$_4$F (sample B, Figure 5b) using a mixing time of 10 ms reveals dipole-dipole interactions between crystallographic **Li**VPO$_4$F and the other paramagnetic ^{7}Li environments, establishing their sub-nanometer-scale proximities within the crystal structure. 2D correlated signals are observed between ^{7}Li signals at 113 and 3 ppm (red solid lines) associated with **Li**VPO$_4$F and environment '*a*', respectively, establishing their dipole-dipole interactions and hence sub-nanometer-scale proximities. Similar 2D correlations exist between **Li**VPO$_4$F and ^{7}Li signals centered at ca. 82 (green solid lines) and at 178 ppm (blue solid lines) associated with environments '*b*' and '*c*', respectively. In addition, broad 2D correlated signals exist between **Li**VPO$_4$F and the unresolved ^{7}Li signal centered at ca. 155 ppm (black solid lines). As expected, no 2D correlations exist between **Li**VPO$_4$F and the ^{7}Li signal at -1 ppm associated with the diamagnetic **Li**F impurity, consistent with their physical separation into different domains. The star-shaped 2D signal of **Li**F is similar to that of **Li**VPO$_4$F and is due to its higher signal-to-noise ratio, compared to the 2D ^{7}Li{^{7}Li} EXSY spectrum, as it is less affected by the additional relaxation contributions that occur under fp-RFDR. Note that variable-temperature ^{7}Li NMR experiments reveal that the paramagnetic ^{7}Li NMR shifts scale linearly with the bulk magnetic susceptibility of LiVPO$_4$F, behavior that further corroborates their existence as defects in the crystal structure (Figure S8, Supporting Information). Thus, the 2D ^{7}Li{^{7}Li} fp-RFDR dipolar correlation NMR spectrum establishes unambiguously that the other paramagnetic ^{7}Li environments are defects within the crystal structure and are not associated with amorphous paramagnetic impurities.

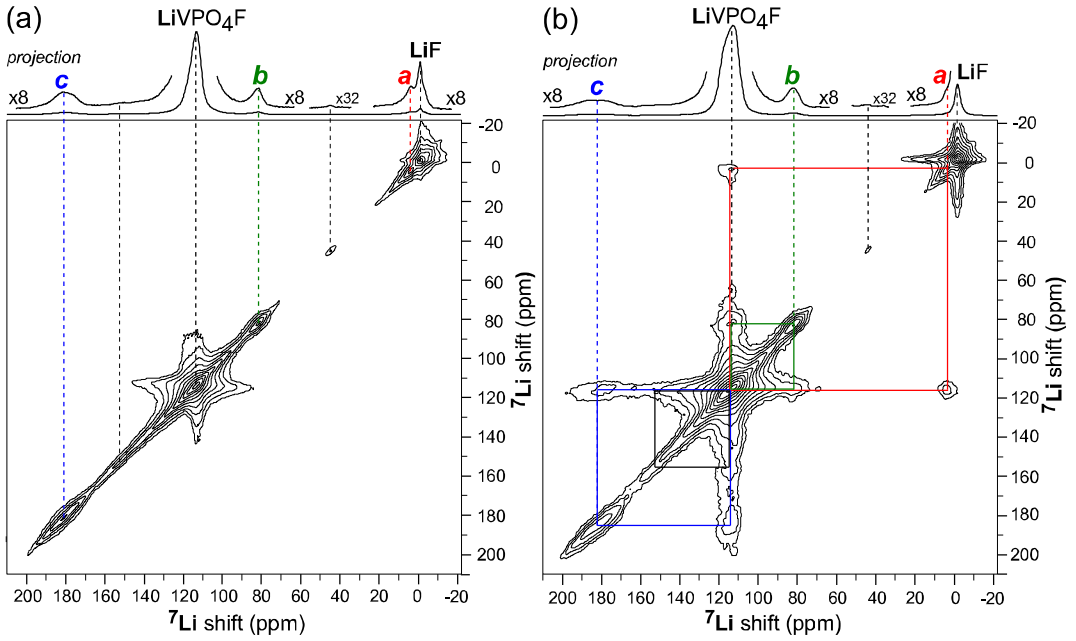

Figure 5. Solid-state (a) 2D ^{7}Li{^{7}Li} EXSY and (b) 2D ^{7}Li{^{7}Li} fp-RFDR dipolar correlation NMR spectra of LiVPO$_4$F (sample B), acquired using mixing times of 10 ms under conditions of 64 kHz MAS and 17.62 T at sample temperatures of 333 K. Skyline projects are shown along the horizontal axes. In (b), solid lines indicate correlated 2D signals between crystallographic **Li**VPO$_4$F and the other paramagnetic ^{7}Li environments, establishing their respective ^{7}Li dipole-dipole interactions and hence sub-nanometer-scale proximities.

To further investigate the proximities among the different lithium defect environments in LiVPO$_4$F, we implemented site-selective ^{7}Li fp-RFDR NMR experiments (Figure 1c). Here, selective excitation of a ^{7}Li defect signal and subsequent application of a broadband ^{7}Li fp-RFDR pulse train enables the through-space transfer of magnetization from the selected ^{7}Li spins to their dipole-dipole-coupled ^{7}Li spins. Such experiments can have certain advantages over 2D ^{7}Li{^{7}Li} fp-RFDR dipolar correlation NMR spectra, as specific interactions among weak ^{7}Li signals—such as defect environments each comprising <5% of the total lithium content—are easier to detect within a constrained experimental time.[39,40] These experiments also permit the analyses of dipolar magnetization transfer originating solely from ^{7}Li spins in the selected environment. Lastly, for ^{7}Li NMR spectra of paramagnetic solids where the isotropic ^{7}Li NMR shifts are separated by frequencies greater than the MAS rate, spectral folding would be observed in 2D correlation experiments, but not in 1D spectra.

Solid-state site-selective ^{7}Li fp-RFDR NMR experiments were acquired on phase-pure $LiVPO_4F$ (sample A) by selectively exciting ^{7}Li spins associated with defect environments '*a*', '*b*', or '*c*', revealing insights into their relative sub-nanometer-scale proximities. For example, compared to the ^{7}Li spin-echo MAS spectrum (Figure 6a), a site-selective ^{7}Li fp-RFDR spectrum acquired with selective excitation of defect environment '*c*' and a mixing time of 0 ms (Figure 6b) results in ^{7}Li signals associated only with '*c*' and its entire spinning-sideband manifold, consistent with the absence of dipolar recoupling. However, an otherwise identical NMR spectrum acquired with a ^{7}Li fp-RFDR mixing time of 10 ms (Figure 6c) reveals the appearance of ^{7}Li signals associated with **Li**VPO_4F, '*a*', and '*b*'. This dipolar transfer of ^{7}Li magnetization, which originates selectively from '*c*', establishes that this lithium defect environment exhibits dipole-dipole couplings and hence sub-nanometer-scale proximities with **Li**VPO_4F (black), '*a*' (red), and '*b*' (green) within the crystal structure. Thus, defect environment '*c*' is not only in close atomic-scale proximity with crystallographic **Li**VPO_4F, as revealed by the 2D ^{7}Li{^{7}Li} fp-RFDR NMR spectrum (Figure 5b), but also to defect environments '*a*' and '*b*'.

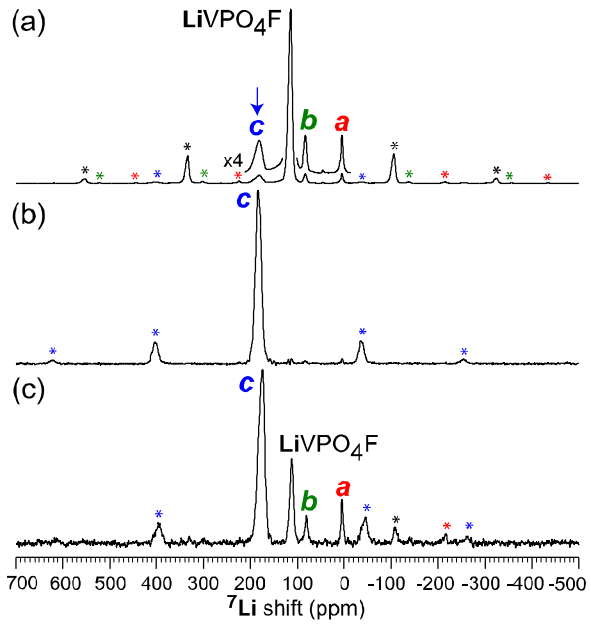

Figure 6. Selective excitation of ^{7}Li spins associated with defect environment '*c*' in phase-pure $LiVPO_4F$ (sample A) and subsequent through-space transfer of magnetization by fp-RFDR to its dipole-dipole-coupled ^{7}Li spins. (a) Solid-state ^{7}Li spin-echo MAS NMR spectrum (identical to Figure 4a). Site-selective ^{7}Li fp-RFDR NMR spectra acquired with (b) 0 and (c) 10 ms mixing times. Asterisks indicate spinning sidebands and are color coded to correspond to the different lithium environments.

Similarly, site-selective ^{7}Li fp-RFDR NMR experiments were performed by selectively exciting lithium defect environment '*a*'. Compared to the ^{7}Li spin-echo MAS NMR spectrum (Figure 7a), a site-selective ^{7}Li fp-RFDR spectrum acquired with a mixing time of 0 ms (Figure 7b) results in ^{7}Li signals associated only with '*a*' and its spinning-sideband manifold, as above. However, an otherwise identical NMR spectrum acquired with a ^{7}Li fp-RFDR mixing time of 10 ms (Figure 7c) reveals ^{7}Li signals intensities associated with **Li**VPO_4F and '*c*', but not '*b*'. Thus, lithium defect environment '*a*' is dipole-dipole-coupled and in close proximity with both **Li**VPO_4F and '*c*', but exhibits a longer separation distance within the crystal structure with respect to defect environment '*b*'.

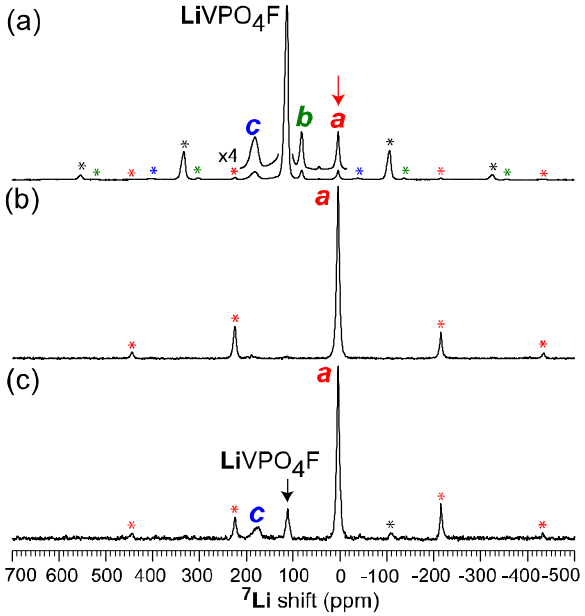

Figure 7. Selective excitation of ^{7}Li spins associated with defect environment '*a*' in phase-pure $LiVPO_4F$ (sample A) and subsequent through-space transfer of magnetization by fp-RFDR to its dipole-dipole-coupled ^{7}Li spins. (a) Solid-state ^{7}Li spin-echo MAS NMR spectrum (identical to Figure 4a). Site-selective ^{7}Li fp-RFDR NMR spectra acquired with (b) 0 and (c) 10 ms mixing times. Asterisks indicate spinning sidebands and are color coded to correspond to the different lithium environments.

Site-selective ^{7}Li fp-RFDR NMR experiments acquired by selectively exciting lithium defect environment '*b*' reveal the appearance of ^{7}Li signals associated with **Li**VPO_4F and '*c*', but not '*a*' (Figure S9, Supporting Information). These results are fully consistent with the above site-selective ^{7}Li fp-RFDR experiments, which show that '*b*' is dipole-dipole coupled to **Li**VPO_4F and '*c*' (Figures 6c), but not '*a*' (Figures 7c).

The site-selective ^{7}Li fp-RFDR NMR experiments were acquired with different dipolar mixing times, enabling analyses of the ^{7}Li magnetization associated with the different lithium environments during fp-RFDR. For every mixing time, the relative magnetization of each

^{7}Li signal was measured by normalizing its intensity (integrated area) with respect to the total spectrum intensity. For the selective excitation of defect environment '*c*' (Figure 8a), ^{7}Li magnetization associated with '*c*' (blue) decreases and magnetization associated with **Li**VPO_4F (black), '*a*' (red), and '*b*' (green) subsequently increase with the dipolar mixing time. The transfer of ^{7}Li magnetization from '*c*' to **Li**VPO_4F, '*a*', and '*b*' over all of the mixing times used here establishes unambiguously their mutual sub-nanometer-scale proximities. Notably, the appearance of NMR signals associated with **Li**VPO_4F, '*a*', and '*b*' after only 1 ms strongly suggests that '*c*' transfers magnetization directly to these environments during fp-RFDR. Note that only direct (and not relayed) transfer of magnetization was observed between ^{13}C nuclei in a ^{13}C-labeled peptide at a mixing time of 1 ms.[24] For the selective excitation of lithium defect environment '*a*' (Figure 8b), ^{7}Li magnetization associated with '*a*' (red) decreases and ^{7}Li magnetization associated with **Li**VPO_4F (black) and '*c*' (blue) subsequently increases over the range of dipolar mixing times. Notably, ^{7}Li magnetization associated with lithium defect environment '*b*' was not observed, even at the longest time used here (15 ms, limited by paramagnetic relaxation processes), establishing the absence of ^{7}Li dipolar couplings and longer separation distance between defect environments '*a*' and '*b*'.

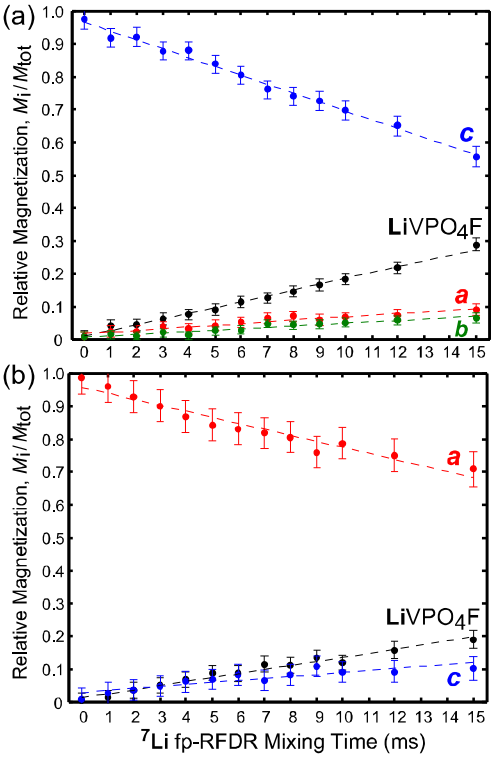

Figure 8. Relative ^{7}Li magnetization associated with the different lithium environments in phase-pure $LiVPO_4F$ (sample A) as a function of diplolar mixing time, obtained from a series of site-selective ^{7}Li fp-RFDR NMR spectra acquired by selectively exciting (a) defect environment '*c*' and (b) defect environment '*a*'. Dashed lines indicate linear fits and uncertainty bars represent 95% confidence intervals.

Interestingly, the relative ^{7}Li magnetization of each of the different environment scales linearly (Figure 9, dashed lines) with the ^{7}Li fp-RFDR dipolar mixing time. Thus, the build-up curves do not exhibit the characteristic dipolar oscillations typical of isolated pairs of spin-1/2 nuclei, which may be a result of (i) the many-body ^{7}Li spin system (92.4% natural abundance), (ii) the complicated ^{7}Li spin dynamics associated with zero-quantum dipolar recoupling in quadrupolar (spin-3/2) nuclei, and (iii) the fast paramagnetic relaxation processes, which do not permit longer dipolar recoupling times. Analogous plots of the absolute (as opposed to relative) ^{7}Li magnetization reveal that additional relaxation processes occur during fp-RFDR (see Figure S10, Supporting Information).

Collectively, the solid-state site-selective ^{7}Li NMR fp-RFDR measurements suggest that environment '*c*' is the result of overlapping contributions of two different defects, 'c_1' and 'c_2', where 'c_1' and '*a*' form a characteristic dipole-dipole-coupled pair, and 'c_2' and '*b*' form another. In fact, environment '*c*' in the solid-state spin-echo ^{7}Li NMR spectra (Figures 4b,c) appears to have an anisotropy in its line shape indicative of two distinct ^{7}Li NMR signals, although the difference between their NMR shifts is too small to separate the ^{7}Li signal into two unique components. It is further possible that 'c_1' and 'c_2' are themselves dipole-dipole coupled, resulting in relative through-space proximities among the environments of '*a*' – 'c_1' – 'c_2' – '*b*', but where the internuclear distance between environments '*a*' and '*b*' is too great for relayed dipolar transfer of magnetization between them over 15 ms of fp-RFDR. The existence of two characteristic dipole-dipole-coupled pairs of lithium defect environments is consistent with their relative ^{7}Li populations. For phase-pure $LiVPO_4F$ (sample A), recall that the ^{7}Li signals associated with '*a*', '*b*', and '*c*' account for 4%, 3%, and 8% of the total lithium content, where the sum of the populations of '*a*' and '*b*' are within experimental error of the population of '*c*'. For $LiVPO_4F$ with minor impurities (sample B), the ^{7}Li signals associated with '*a*', '*b*', and '*c*' account for 2%, 2%, and 4% of the total lithium content, where the sum of the populations of '*a*' and '*b*' are equal to the population of '*c*'.

While we prove the existence of high concentrations of characteristic lithium defect environments in $LiVPO_4F$ and identify their relative proximities, identifying their physicochemical origins is still a topic of ongoing research. The different ^{7}Li Fermi contact shifts of the defect environments establish that each one exhibits a local electronic environment that is distinct from crystallographic lithium in defect-free regions of $LiVPO_4F$. Because the Fermi contact interaction depends on

unpaired electron spin polarization, the different lithium defect environments are a result of altered oxidation and/or spin states of nearby paramagnetic vanadium atoms, which in turn could have different possible origins. For example, it is possible that some or all of the defect environments result from the local substitution of an oxygen atom for a fluorine atom, which would change the oxidation state of a vanadium atom (formally, V^{3+} to V^{4+}); note that $LiVPO_4O$ is a known crystal structure.[19] Similarly, because the vanadium atoms can exhibit multiple oxidation states, it is also possible that the defects are the result of a local excess or vacancy of lithium atoms (resulting in V^{2+} and V^{4+}, respectively). DFT calculations of the ^{7}Li Fermi contact shifts of model defects within $LiVPO_4F$ are in progress, which are expected to yield additional insights into their physicochemical nature.

CONCLUSION

Well-crystallized $LiVPO_4F$ samples were synthesized with the expected tavorite-like crystal structure, as established by XRD and STEM measurements. Solid-state ^{7}Li spin-echo NMR measurements reveal the existence of unexpected ^{7}Li environments that can account for up to 20% of the total lithium content, where their NMR shifts and relaxation rates indicate that they are paramagnetic. 2D ^{7}Li{^{7}Li} fp-RFDR dipolar correlation NMR experiments establish the atomic-scale proximities of lithium in each environment with respect to lithium in the $LiVPO_4F$ crystallographic site, proving unambiguously that the unexpected lithium environments are associated with defects in the crystal structure and are not amorphous impurity phases.. Site-selective ^{7}Li fp-RFDR NMR experiments establish the relative proximities among the lithium defect environments, revealing the existence of two characteristic dipole-dipole-coupled pairs. The different ^{7}Li Fermi contact shifts of the lithium defects establish that they exhibit local electronic environments distinct from lithium in the crystallographic $LiVPO_4F$ site, which are directly linked to the electronic environments (and hence, oxidation and spin states) of nearby paramagnetic vanadium atoms.

More generally, we show that ^{7}Li fp-RFDR dipolar correlation NMR experiments can be performed on paramagnetic solids with fast ^{7}Li NMR relaxation times on the order of milliseconds, opening the application of such NMR experiments to paramagnetic lithium-ion battery materials. The results also highlight the high sensitivity of solid-state NMR to interactions between nuclear and unpaired electron spins, as the existence of relatively high concentrations of paramagnetic lithium defect environments is compatible with the long-range average structure of $LiVPO_4F$, as measured by diffraction. The characterization strategy presented here is not only useful for identifying defects in lithium-containing crystalline solids, such as lithium-ion intercalation electrodes, but also can be applied to better understand local lithium environments in amorphous materials.

ASSOCIATED CONTENT

Supporting Information. Rietveld refinement of XRD pattern; additional STEM images; EELS analyses; solid-state ^{6}Li, ^{19}F, and ^{31}P NMR spectra; ^{7}Li NMR shifts vs. bulk magnetic susceptibility; additional site-selective ^{7}Li fp-RFDR NMR spectra and analyses. This material is available free of charge on the ACS Publications website at http://pubs.acs.org.

AUTHOR INFORMATION

Corresponding Author

*michael.deschamps@cnrs-orleans.fr

Notes

The authors declare no competing financial interests.

ACKNOWLEDGMENT

R.J.M. gratefully acknowledges support from a Marie Curie Postdoctoral Fellowship through the European Union Seventh Framework Programme (FP7/2007-2013) under grant agreement 330735. J.M.A.M. gratefully acknowledges the European Research Network ALISTORE-ERI for a Ph.D. grant. We thank Région Aquitaine and the TGIR-RMN-THC (Fr3050 CNRS) for additional financial support, J. Humez for technical assistance, and Dr. F. Fayon for fruitful discussions.

REFERENCES

(1) Armand, M.; Tarascon, J.-M. Building Better Batteries. *Nature* **2008**, *451*, 652–657.

(2) Grey, C. P.; Dupré, N. NMR Studies of Cathode Materials for Lithium-Ion Rechargeable Batteries. *Chem. Rev.* **2004**, *104*, 4493–4512.

(3) Böhmer, R.; Jeffrey, K. R.; Vogel, M. Solid-State Li NMR with Applications to the Translational Dynamics in Ion Conductors. *Prog. Nucl. Mag. Res. Sp.* **2007**, *50*, 87–174.

(4) Carlier, D.; Ménétrier, M.; Grey, C.; Delmas, C.; Ceder, G. Understanding the NMR Shifts in Paramagnetic Transition Metal Oxides Using Density Functional Theory Calculations. *Phys. Rev. B* **2003**, *67*, 174103.

(5) Zhang, Y.; Castets, A.; Carlier, D.; Menetrier, M.; Boucher, F. Simulation of NMR Fermi Contact Shifts for Lithium Battery Materials: the Need for an Efficient Hybrid Functional Approach. *J. Phys. Chem. C* **2012**, *116*, 17393–17402.

(6) Dogan, F.; Long, B. R.; Croy, J. R.; Gallagher, K. G.; Iddir, H.; Russell, J. T.; Balasubramanian, M.; Key, B. Re-Entrant Lithium Local Environments and Defect Driven Electrochemistry of Li- and Mn-Rich Li-Ion Battery Cathodes. *J. Am. Chem. Soc.* **2015**, *137*, 2328–2335.

(7) Chazel, C.; Menetrier, M.; Croguennec, L.; Delmas, C. $^{6/7}$Li NMR Study of the $Li_{1-z}Ni_{1+z}O_2$ Phas-

es. *Magn. Reson. Chem.* **2005**, *43*, 849–857.
(8) Levasseur, S.; Menetrier, M.; Shao-Horn, Y.; Gautier, L.; Audemer, A.; Demazeau, G.; Largeteau, A.; Delmas, C. Oxygen Vacancies and Intermediate Spin Trivalent Cobalt Ions in Lithium-Overstoichiometric $LiCoO_2$. *Chem. Mater.* **2003**, *15*, 348–354.
(9) Murakami, M.; Noda, Y.; Koyama, Y.; Takegoshi, K.; Arai, H.; Uchimoto, Y.; Ogumi, Z. Local Structure and Spin State of Cobalt Ion at Defect in Lithium Overstoichiometric $LiCoO_2$ As Studied by $^{6/7}$Li Solid-State NMR Spectroscopy. *J. Phys. Chem. C* **2014**, *118*, 15375-15385.
(10) Pourpoint, F.; Hua, X.; Middlemiss, D. S.; Adamson, P.; Wang, D.; Bruce, P. G.; Grey, C. P. New Insights Into the Crystal and Electronic Structures of $Li_{1+x}V_{1-x}O_2$ from Solid State NMR, Pair Distribution Function Analyses, and First Principles Calculations. *Chem. Mater.* **2012**, *24*, 2880–2893.
(11) Hohwy, M.; Jakobsen, H. J.; Eden, M.; Levitt, M. H.; Nielsen, N. C. Broadband Dipolar Recoupling in the Nuclear Magnetic Resonance of Rotating Solids: a Compensated C_7 Pulse Sequence. *J. Chem. Phys.* **1998**, *108*, 2686–2694.
(12) Bennett, A. E.; Rienstra, C. M.; Griffiths, J. M.; Zhen, W.; Lansbury, P. T.; Griffin, R. G. Homonuclear Radio Frequency-Driven Recoupling in Rotating Solids. *J. Chem. Phys.* **1998**, *108*, 9463-9479.
(13) Ishii, Y.; (null). ^{13}C–^{13}C Dipolar Recoupling Under Very Fast Magic Angle Spinning in Solid-State Nuclear Magnetic Resonance: Applications to Distance Measurements, Spectral Assignments, and High-Throughput Secondary-Structure Determination. *J. Chem. Phys.* **2001**, *114*, 8473-8483.
(14) Nielsen, N. C.; Bildso, H.; Jakobsen, H. J.; Levitt, M. H. Double^Quantum Homonuclear Rotary Resonance: Efficient Dipolar Recovery in Magic^ Angle Spinning Nuclear Magnetic Resonance. *J. Chem. Phys.* **1994**, *101*, 1805–1812.
(15) Spencer, T. L.; Plagos, N. W.; Brouwer, D. H.; Goward, G. R. The Use of ^{6}Li{^{7}Li}-REDOR NMR Spectroscopy to Compare the Ionic Conductivities of Solid-State Lithium Ion Electrolytes. *Phys. Chem. Chem. Phys.* **2014**, *16*, 2515–2526.
(16) van Wüllen, L.; Echelmeyer, T.; Meyer, H.-W.; Wilmer, D. The Mechanism of Li-Ion Transport in the Garnet $Li_5La_3Nb_2O_{12}$. *Phys. Chem. Chem. Phys.* **2007**, *9*, 3298-3303.
(17) Barker, J.; Saidi, M. Y.; Swoyer, J. Lithium Metal Fluorophosphate Materials and Preparation Thereof. 6,387,568, May 14, 2002.
(18) Ateba Mba, J.-M.; Croguennec, L.; Basir, N. I.; Barker, J.; Masquelier, C. Lithium Insertion or Extraction From/Into Tavorite-Type $LiVPO_4F$: an *in Situ* X-Ray Diffraction Study. *J. Electrochem. Soc.* **2012**, *159*, A1171–A1175.
(19) Ateba Mba, J.-M.; Masquelier, C.; Suard, E.; Croguennec, L. Synthesis and Crystallographic Study of Homeotypic $LiVPO_4F$ and $LiVPO_4O$. *Chem. Mater.* **2012**, *24*, 1223–1234.
(20) Ellis, B. L.; Ramesh, T. N.; Davis, L. J.; Goward, G. R.; Nazar, L. F. Structure and Electrochemistry of Two-Electron Redox Couples in Lithium Metal Fluorophosphates Based on the Tavorite Structure. *Chem. Mater.* **2011**, *23*, 5138–5148.
(21) Masquelier, C.; Croguennec, L. Polyanionic (Phosphates, Silicates, Sulfates) Frameworks as Electrode Materials for Rechargeable Li (or Na) Batteries. *Chem. Rev.* **2013**, *113*, 6552–6591.
(22) Bielecki, A.; Burum, D. P. Temperature Dependence of ^{207}Pb MAS Spectra of Solid Lead Nitrate. an Accurate, Sensitive Thermometer for Variable-Temperature MAS. *J. Magn. Reson. Ser. A* **1995**, *116*, 215–220.
(23) Massiot, D.; Fayon, F.; Capron, M.; King, I.; Calve, S. L.; Alonso, B.; Durand, J.-O.; Bujoli, B.; Gan, Z.; Hoatson, G. Modelling One- and Two-Dimensional Solid-State NMR Spectra. *Magn. Res. Chem.* **2001**, *40*, 70–76.
(24) Shen, M.; Hu, B.; Lafon, O.; Trébosc, J.; Chen, Q.; Amoureux, J.-P. Broadband Finite-Pulse Radio-Frequency-Driven Recoupling (fp-RFDR) with $(XY8)4^1$ Super-Cycling for Homo-Nuclear Correlations in Very High Magnetic Fields at Fast and Ultra-Fast MAS Frequencies. *J. Magn. Reson.* **2012**, *223*, 107–119.
(25) States, D. J.; Haberkorn, R. A.; Ruben, D. J. A Two-Dimensional Nuclear Overhauser Experiment with Pure Absorption Phase in Four Quadrants. *J. Magn. Reson.* **1982**, *48*, 286–292.
(26) Kupce, E.; Boyd, J.; Campbell, I. D. Short Selective Pulses for Biochemical Applications. *J. Magn. Reson. Ser. B* **1995**, *106*, 300–303.
(27) Fitting Kourkoutis, L.; Hotta, Y.; Susaki, T.; Hwang, H.; Muller, D. Nanometer Scale Electronic Reconstruction at the Interface Between $LaVO_3$ and $LaVO_4$. *Phys. Rev. Lett.* **2006**, *97*, 256803.
(28) Li, J.; Gauntt, B. D.; Kulik, J.; Dickey, E. C. Stoichiometry of Nanocrystalline VOx Thin Films Determined by Electron Energy Loss Spectroscopy. *Microsc. Microanal.* **2009**, *15*, 1004–1005.
(29) Castets, A. RMN De Matériaux Paramagnétiques: Mesures Et Modélisation, Université Bordeaux 1, 2011, pp. 1–215.
(30) Duttine, M.; Carlier, D.; Ateba Mba, J.-M.; Croguennec, L.; Masquelier, C.; Ménétrier, M. ^{19}F, ^{7}Li and ^{31}P MAS NMR Characterization and DFT Calculations for the Tavorite $LiVPO_4F$. In; Arcachon, 2013.
(31) Kosova, N. V.; Devyatkina, E. T.; Slobodyuk, A. B.; Gutakovskii, A. K. $LiVPO_4F/Li_3V_2(PO_4)_3$ Nanostructured Composite Cathode Materials Prepared via Mechanochemical Way. *J. Solid State Electrochem.* **2013**, *18*, 1389–1399.
(32) Reimer, L.; Zepke, U.; Moesch, J.; Schulze-Hillert, S. T.; Ross-Messemer, M.; Probst, W.;

Weimer, E. EELS Spectroscopy: a Reference Handbook of Standard Data for Identification and Interpretation of Electron Energy Loss Spectra and for Generation of Electron Spectroscopic Images; Electron Optics Division, C. Z., Ed.; Oberkochen, Germany, 1992.

(33) Gunther, H. Lithium NMR. In *Encyclopedia of Nuclear Magnetic Resonance*; John Wiley & Sons, Ltd: Chichester, 2007; pp. 1–21.

(34) Bertini, I.; Luchinat, C.; Parigi, G. Magnetic Susceptibility in Paramagnetic NMR. *Prog. Nucl. Mag. Res. Sp.* **2002**, *40*, 249–273.

(35) Cahill, L. S.; Chapman, R. P.; Britten, J. F.; Goward, G. R. 7Li NMR and Two-Dimensional Exchange Study of Lithium Dynamics in Monoclinic $Li_3V_2(PO_4)_3$. *The Journal of Physical Chemistry B* **2006**, *110*, 7171–7177.

(36) Castets, A.; Carlier, D.; Trad, K.; Delmas, C.; Ménétrier, M. Analysis of the ^{7}Li NMR Signals in the Monoclinic $Li_3Fe_2(PO_4)_3$ and $Li_3V_2(PO_4)_3$ Phases. *J. Phys. Chem. C* **2010**, *114*, 19141–19150.

(37) Davis, L. J. M.; Heinmaa, I.; Goward, G. R. Study of Lithium Dynamics in Monoclinic $Li_3Fe_2(PO_4)_3$ using ^{6}Li VT and 2D Exchange MAS NMR Spectroscopy. *Chem. Mater.* **2010**, *22*, 769–775.

(38) Bennett, A. E.; Griffin, R. G.; Ok, J. H.; Vega, S. Chemical Shift Correlation Spectroscopy in Rotating Solids: Radio Frequency-Driven Dipolar Recoupling and Longitudinal Exchange. *J. Chem. Phys.* **1992**, *96*, 8624-8627.

(39) Alonso, B.; Fayon, F.; Massiot, D.; Amenitsch, H.; Malfatti, L.; Kidchob, T.; Costacurta, S.; Innocenzi, P. Hybrid Organic-Inorganic Mesostructured Membranes: Interfaces and Organization at Different Length Scales. *J. Phys. Chem. C* **2010**, *114*, 11730–11740.

(40) Davis, L. J. M.; Ellis, B. L.; Ramesh, T. N.; Nazar, L. F.; Bain, A. D.; Goward, G. R. ^{6}Li 1D EXSY NMR Spectroscopy: a New Tool for Studying Lithium Dynamics in Paramagnetic Materials Applied to Monoclinic Li_2VPO_4F. *J. Phys. Chem. C* **2011**, *115*, 22603–22608.

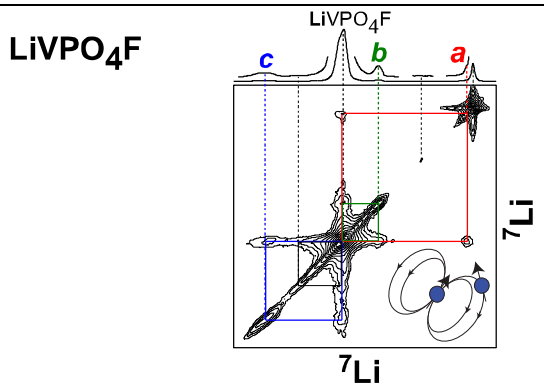

Insert Table of Contents artwork here

SUPPORTING INFORMATION

Revealing Defects in Crystalline Lithium-Ion Battery Electrodes by Solid-State NMR: Applications to $LiVPO_4F$

Robert J. Messinger, Michel Ménétrier, Elodie Salager, Adrien Boulineau, Mathieu Duttine, Dany Carlier, Jean-Marcel Ateba Mba, Laurence Croguennec, Christian Masquelier, Dominique Massiot, Michaël Deschamps

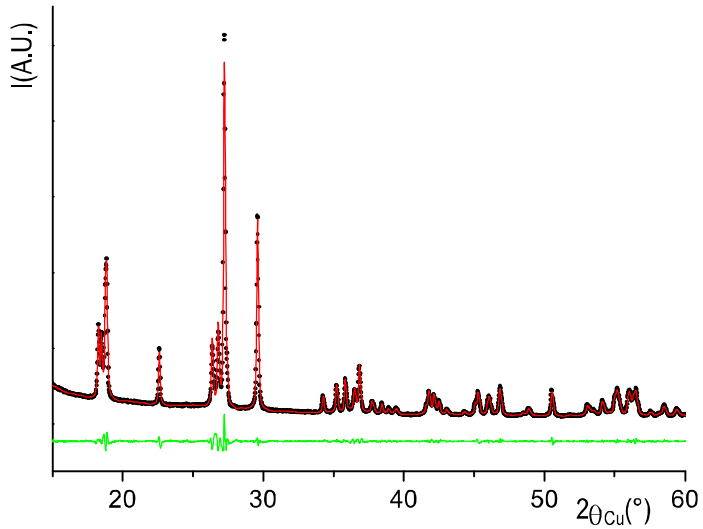

Figure S1. Rietveld refinement of the X-ray diffractogram of phase-pure $LiVPO_4F$ (sample A) with respect to the tavorite-like structure of $LiVPO_4F$. Experimental and refined XRD patterns are shown in black and red, respectively, with the difference between them shown in green.

$LiVPO_4F$

S.G. : P-*1*; Z = 2
a **= 5.1708(3) Å; *b* = 5.3083(3) Å; *c* = 7.2631(4) Å;**
α = 107.595(3) °; β = 107.969(2) °; γ = 98.388(2) °
V = 174.36(2) Å^3; V/Z = 87.18 Å^3

X-Ray: R_{wp} = 15.2%;
R_{bragg} = 1.88% χ^2 = 1.73

Atomic parameters

Atoms	Wyckoff position	Atomic position			Occ	B_{iso}
		x/a	*y/b*	*z/c*		
V(1)	1a	0	0	0	1	0.40(1)
V(2)	1b	0	0	1/2	1	0.31(1)
P	2i	0.3264(1)	0.6494(1)	0.2533(1)	1	0.56(4)
O(1)	2i	0.3737(3)	0.2374(2)	0.5962(2)	1	0.42(3)
O(2)	2i	0.1072(2)	-0.3218(2)	0.3508(2)	1	0.43(3)
O(3)	2i	0.6906(2)	0.6567(2)	-0.1471(2)	1	0.75(3)
O(4)	2i	0.2567(2)	0.7848(2)	0.0885(2)	1	0.30(2)
F	2i	-0.1135(2)	0.0873(2)	0.2438(2)	1	0.84(3)
Li(1)	2i	0.703(1)	0.371(1)	0.233(1)	1	2.64(2)

Table S1. Crystal structure parameters obtained after Rietveld refinement of the XRD pattern (Figure S1) of phase-pure $LiVPO_4F$ (sample A).

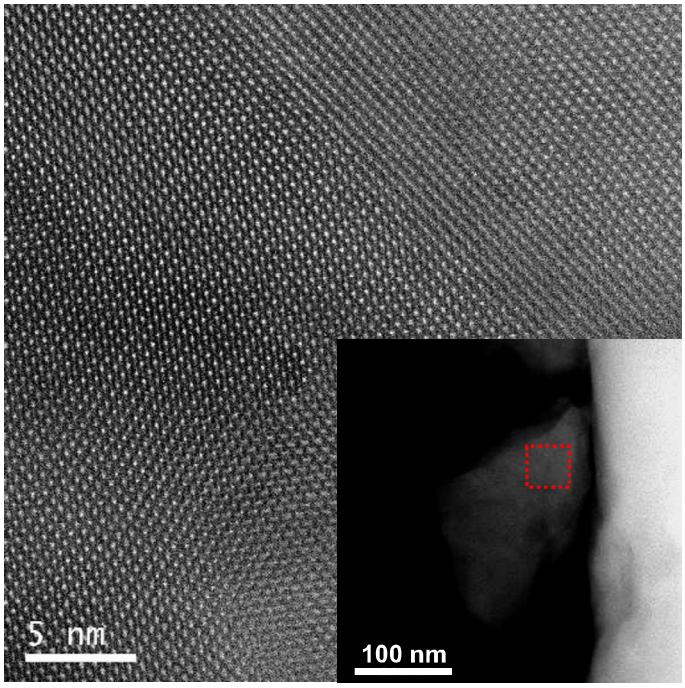

Figure S2. STEM image of phase-pure $LiVPO_4F$ (sample A), revealing a high extent of crystallinity along the [010] axis. *Inset:* $LiVPO_4F$ particle, showing the region (red box) from which the image was acquired.

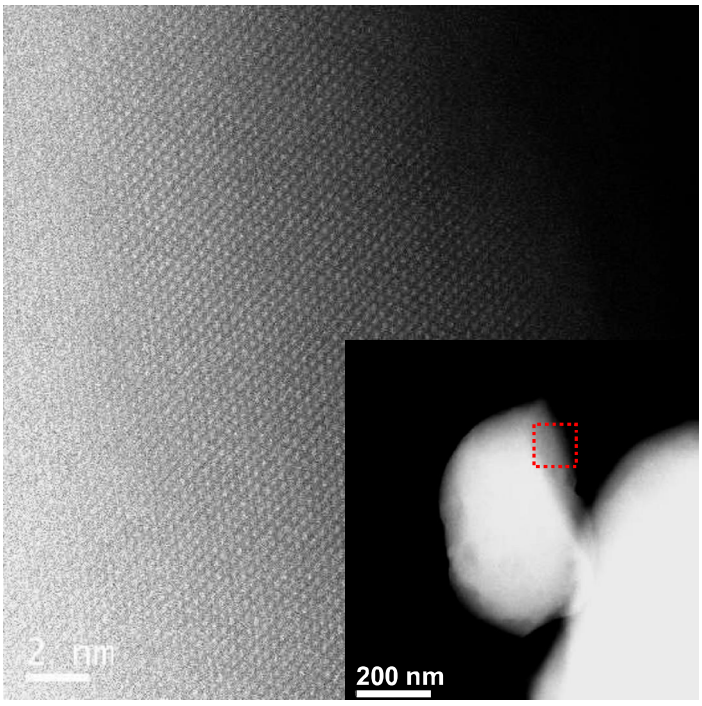

Figure S3. STEM image of phase-pure $LiVPO_4F$ (sample A), revealing a high extent of crystallinity along the [1-21] axis. *Inset:* $LiVPO_4F$ particle, showing the region (red box) from which the image was acquired.

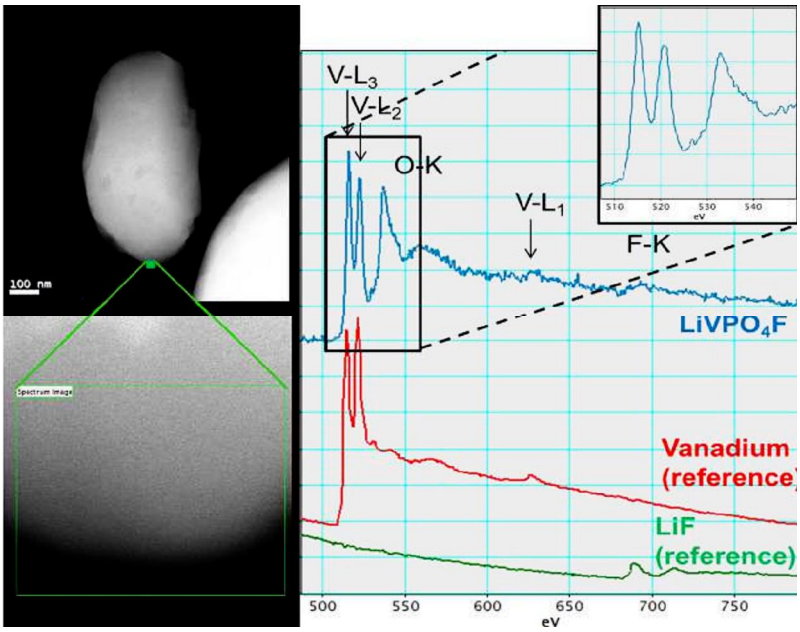

Figure S4. EEL spectrum of phase-pure $LiVPO_4F$ (sample A). The spectrum is the average of those collected within the green rectangle (28 nm x 22 nm) depicted on the left. The inset shows the V-L_3, V-L_2 and beginning of the O-K edges in more detail. EEL spectra of metallic vanadium and LiF are shown for comparison.

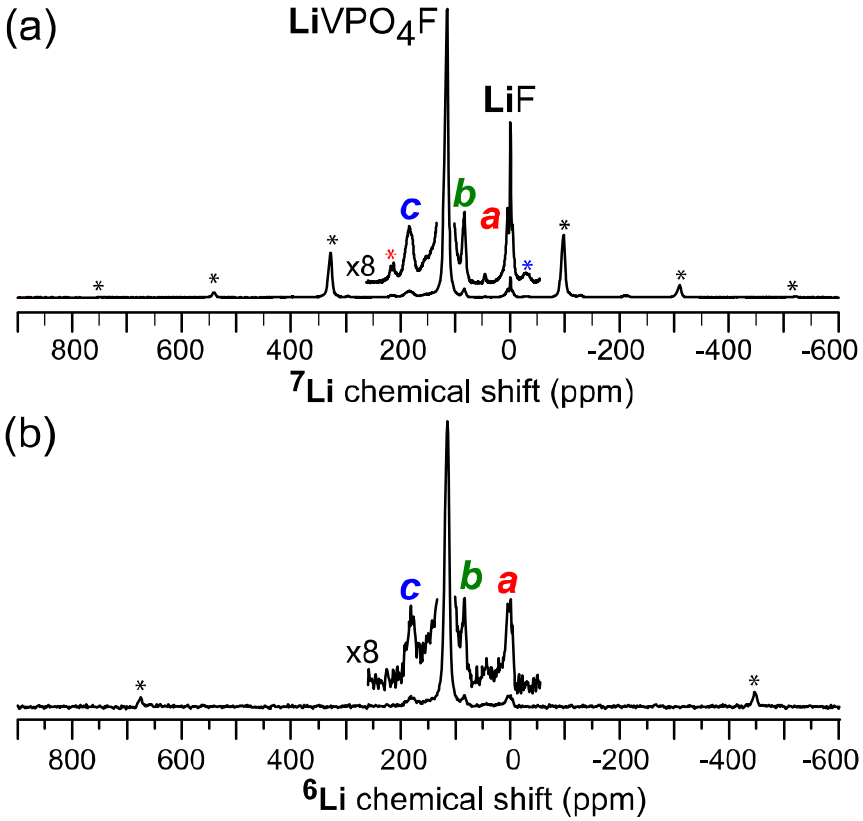

Figure S5. Solid-state (a) ^7Li and (b) ^6Li NMR spin-echo spectra of $LiVPO_4F$ (sample B), acquired under conditions of 64 kHz MAS and 17.62 T at sample temperatures of 333 K. Asterisks indicate spinning sidebands.

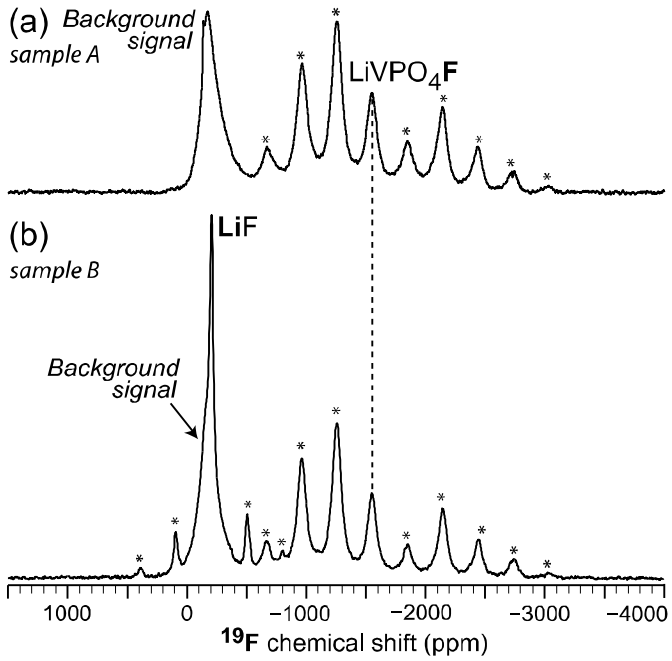

Figure S6. Solid-state ^{19}F spin-echo NMR spectra of (a) phase-pure $LiVPO_4F$ (sample A), and (b) $LiVPO_4F$ with minor impurities (sample B), acquired under conditions of 28 kHz MAS and 2.35 T at sample temperatures of 325 K. Asterisks indicate spinning sidebands. The carrier frequency was centered on the most intense $LiVPO_4F$ sideband at -1250 ppm and does not uniformly excite the entire ^{19}F spinning-sideband manifold. The isotropic ^{19}F signal at -1540 ppm associated with crystallographic $LiVPO_4F$ was determined by variable-temperature NMR experiments.

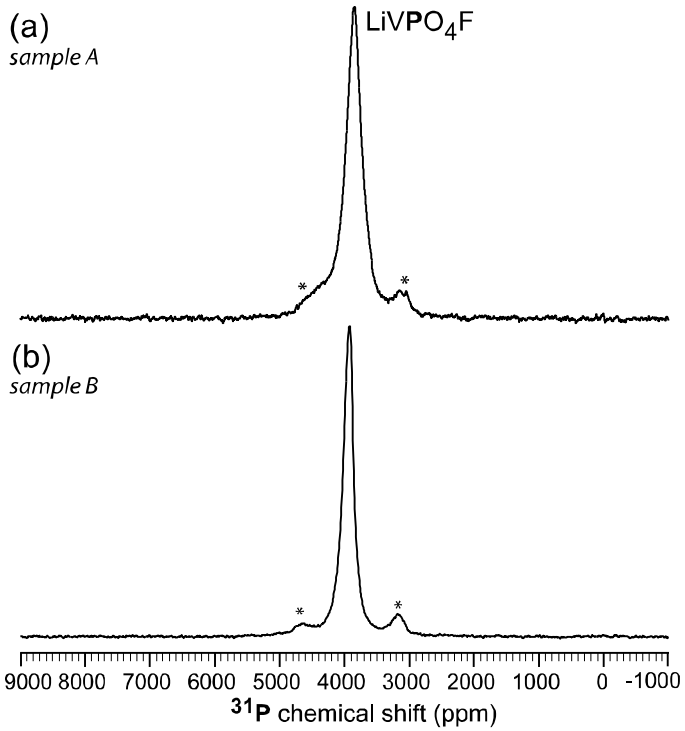

Figure S7. Solid-state ^{31}P spin-echo NMR spectra of (a) phase-pure $LiVPO_4F$ (sample A), and (b) $LiVPO_4F$ with minor impurities (sample B), acquired under conditions of 30 kHz MAS and 2.35 T at sample temperatures of 330 K. Asterisks indicate spinning sidebands.

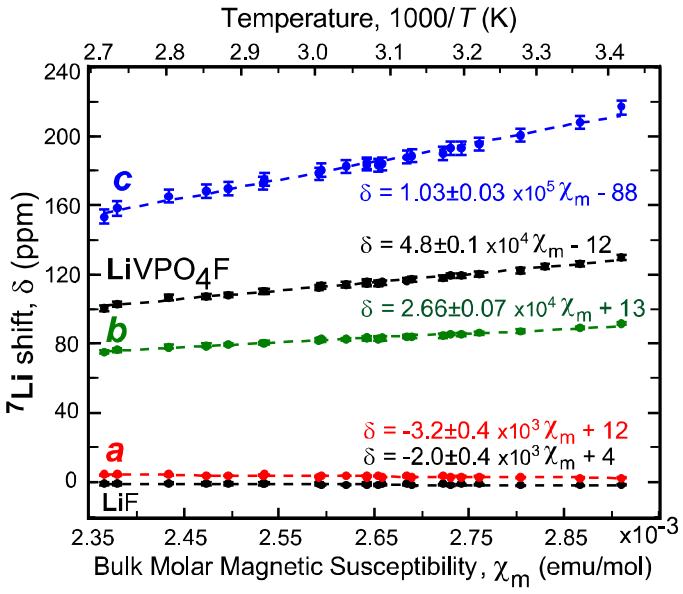

Figure S8. Dependence of ^{7}Li NMR shifts in $LiVPO_4F$ (sample B) vs. the bulk molar magnetic susceptibility (bottom axis) and temperature (top axis). Dashed lines indicate linear fits and uncertainty bars represent 95% confidence intervals.

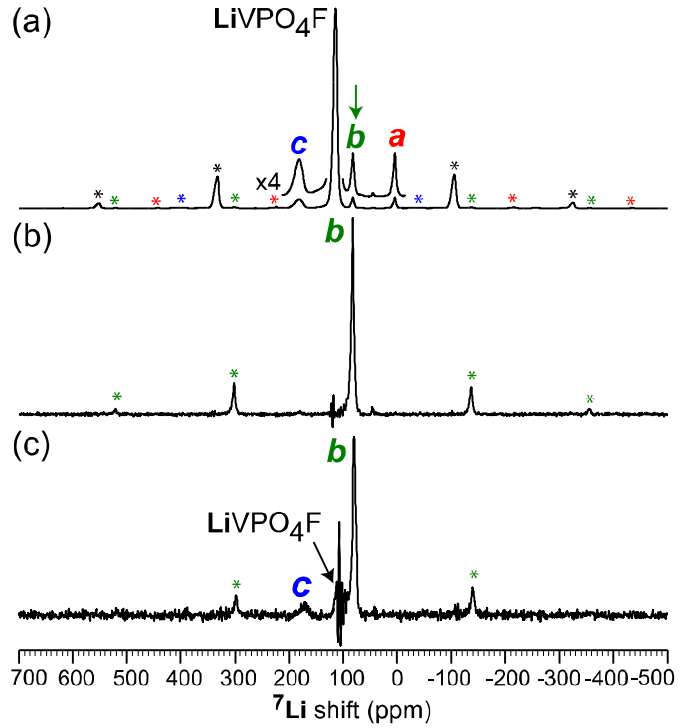

Figure S9. Selective excitation of ^{7}Li spins associated with defect environment '*b*' in phase-pure $LiVPO_4F$ (sample A) and subsequent through-space transfer of magnetization by fp-RFDR to its dipole-dipole-coupled ^{7}Li spins. (a) Solid-state ^{7}Li spin-echo MAS NMR spectrum (identical to Figure 4a in the main article). Site-selective ^{7}Li fp-RFDR spectra acquired with (b) 0 and (c) 10 ms mixing times, where magnetization was stored along the longitudinal axis for a fixed time of 15 ms. The ^{7}Li signal associated with **Li**VPO_4F has a phase distortion due to interference from the selective SNOB-type pulses. Asterisks indicated spinning sidebands and are color coded to correspond to the different lithium environments.

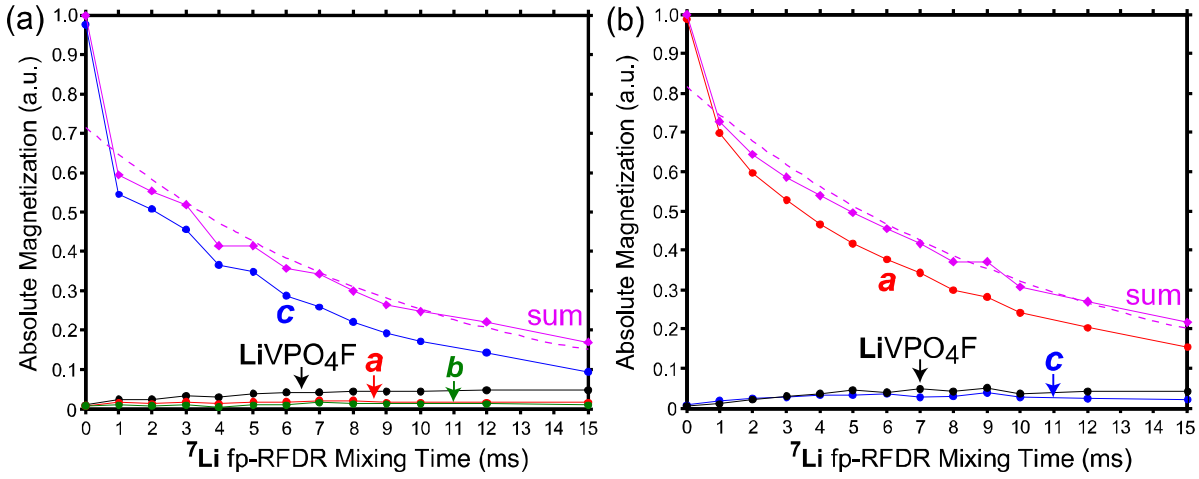

Figure S10. Absolute ^{7}Li magnetization associated with the different lithium environments in phase-pure $LiVPO_4F$ (sample A) as a function of fp-RFDR mixing time, obtained from a series of site-selective ^{7}Li fp-RFDR spectra acquired by initially exciting (a) defect environment '*c*' and (b) defect environment '*a*'. Magnetization was stored along the longitudinal axis for a fixed time of 15 ms. The sum of the ^{7}Li magnetization (magenta points) decays with increasing dipolar mixing time, which can be modeled as a mono-exponential decay (dashed magenta line) with a time constant, T_1^{RFDR}, of 9.6 ms and 10.7 ms for the selective excitation of '*c*' and '*a*', respectively. Additional relaxation associated with ^{7}Li fp-RFDR is likely due to (i) the re-introduction of ^{7}Li homonuclear dipolar interactions, and (ii) increased thermal motions due to sample heating from longer radiofrequency duty cycles.

Discussion of variable-temperature ^{7}Li NMR experiments.

Variable-temperature ^{7}Li NMR measurements were conducted to determine if the ^{7}Li NMR shifts of the paramagnetic defect environments scale linearly with the bulk molar magnetic susceptibility of $LiVPO_4F$ (Figure S8), behavior that would further corroborate their existence as defects in the crystal structure. The Fermi-contact interactions that dominate the NMR shifts of paramagnetic environments are expected to scale linearly with the molar magnetic susceptibility of the bulk material (Bertini, *et al.*, *Prog. Nucl. Mag. Res. Sp.* **2002**, *40*, 249-273). $LiVPO_4F$ exhibits a Curie-Weiss-type paramagnetism over the temperature range investigated here (Ateba Mba, *et al.*, *Chem. Mater.* **2012**, *24*, 1223-1234), where the inverse molar magnetic susceptibility scales linearly with the temperature ($1/\chi_m \sim T$). Indeed, the ^{7}Li NMR shifts of not only crystallographic **Li**VPO_4F, but also the lithium defect environments, scale linearly (dashed lines) with the bulk molar magnetic susceptibility, consistent with their existence in the bulk $LiVPO_4F$ structure. The ratio of the Fermi contact shift to the bulk magnetic susceptibility is proportional to the quantity of unpaired electron spin polarization transferred to the associated nucleus. For example, the slopes are correlated with the magnitudes of the ^{7}Li NMR shifts for environments '*c*', **Li**VPO_4F, and '*b*'. Environment '*a*' has a ^{7}Li shift that exhibits a weak (but statistically significant) negative dependence on the magnetic susceptibility, likely due to competing Fermi contact shift mechanisms (e.g., spin delocalization and polarization). The ^{7}Li shift for the diamagnetic **Li**F impurity exhibits an even weaker negative dependence, possibly due to changes in its lattice constant with temperature. Note that signals arising from separate paramagnetic impurities might also exhibit a similar temperature dependence of their contact shifts if their corresponding structures exhibit a Curie-Weiss-type magnetism over this temperature range.

Additional Experimental Details.

Solid-state ^{6}Li NMR spectroscopy. The solid-state ^{6}Li NMR spectrum was acquired on a Bruker AVANCE III 750 NMR spectrometer with a 17.62 T wide-bore superconducting magnet operating at 291.5 MHz for ^{6}Li nuclei, which are 7.6% naturally abundant. A Bruker ^{1}H/X double-resonance magic-angle-spinning (MAS) probeheads was used with 1.3-mm diameter zirconia rotors, where samples were rotated at 64 MAS with N_2 gas under ambient conditions. The sample temperature was calibrated using $Pb(NO_3)_2$ as a chemical shift thermometer. The ^{6}Li spin-echo MAS NMR spectrum was acquired with a half-echo delay ($\tau/2$) of one rotor period (15.625 μs) using a radiofrequency field strength of 36 kHz ($\pi/2$ pulse of 5.5 μs). A recycle delay of 50 ms was used; note that the diamagnetic LiF impurity did not relax appreciably to thermal equilibrium during this time and its NMR signal was effectively quenched. ^{6}Li NMR shifts were referenced to a 1 M aqueous solution of LiCl at 0 ppm.

Solid-state ^{19}F and ^{31}P NMR spectroscopy Solid-state ^{19}F and ^{31}P NMR spectra were acquired on a Bruker AVANCE III 100 NMR spectrometer with a 2.35 T wide-bore superconducting magnetic operating at 94.3 and 40.6 MHz for ^{19}F and ^{31}P nuclei, respectively, which are both 100 % naturally abundant. Bruker $^{1}H/X$ double-resonance magic-angle-spinning (MAS) probeheads were used with 2.5-mm diameter zirconia rotors, where samples were rotated at 28 kHz (^{19}F) or 30 kHz (^{31}P) MAS with dry air under ambient conditions. Sample temperatures were calibrated using $Pb(NO_3)_2$. ^{19}F and ^{31}P NMR shifts were referenced to $CFCl_3$ and H_3PO_4 (85 wt. %), respectively. All ^{19}F and ^{31}P NMR experiments were conducted using radiofrequency field strengths of 240 kHz ($\pi/2$ pulses of 1.05 μs). Recycle delays of 1 s were used, during which all ^{19}F or ^{31}P nuclei fully relaxed to thermal equilibrium. For the ^{19}F experiments, it was not possible to uniformly excite the entire spinning-sideband manifold using the Hahn spin-echo sequence, even using a short excitation pulse at a low magnetic field strength. Here, the carrier frequency was centered on the most intense spinning sideband of $LiVPO_4F$ at -1250 ppm.

Electron energy loss spectroscopy (EELS). EELS spectra were recorded in spectrum-imaging mode with a Gatan GIF Quantum electron spectrometer. Convergence and collection angles of 21 and 35 mrad were used, respectively. Spectra were recorded with an exposure time of 40 ms to avoid any modification of the material during the experiments. A post-processing technique based on principal component analysis (PCA) was applied to enhance the signal-to-noise ratio of the spectra.